The Astrophysical Journal, 962:28 (17pp), 2024 February 10 https://doi.org/10.3847/1538-4357/ad132a

Multiple Shells Driven by Disk Winds: ALMA Observations in the HH 30 Outflow

J. A. López-Vázquez[17], Chin-Fei Lee[1], M. Fernández-López[2], Fabien Louvet[3,4], O. Guerra-Alvarado[5], and Luis A. Zapata[6]
[1] Academia Sinica Institute of Astronomy and Astrophysics, No. 1, Section 4, Roosevelt Road, Taipei 10617, Taiwan; jlopezv@asiaa.sinica.edu.tw
[2] Instituto Argentino de Radioastronomía (CCT-La Plata, CONICET; CICPBA), C.C. No. 5, 1894, Villa Elisa, Buenos Aires, Argentina
[3] Univ. Grenoble Alpes, CNRS, IPAG, F-38000 Grenoble, France
[4] Departamento de Astronomía, Universidad de Chile, Casilla 36-D, Santiago , Chile
[5] Leiden Observatory, Leiden University, PO Box 9513, 2300 RA Leiden, The Netherlands
[6] Instituto de Radioastronomía y Astrofísica, Universidad Nacional Autónoma de México, Apartado Postal 3-72, 58089 Morelia, Michoacán, México
Received 2023 August 16; revised 2023 December 5; accepted 2023 December 5; published 2024 February 2

Abstract

We present archival Atacama Large Millimeter/submillimeter Array band 6 observations of the ^{13}CO ($J = 2$–1) and ^{12}CO ($J = 2$–1) molecular line emission of the protostellar system associated with HH 30. The ^{13}CO molecular line shows the accretion disk while the molecular outflow is traced by the emission of the ^{12}CO molecular line. We estimated a dynamical mass for the central object of $0.45 \pm 0.14\,M_{\odot}$, and a mass for the molecular outflow of $(1.83 \pm 0.19) \times 10^{-4}\,M_{\odot}$. The molecular outflow presents an internal cavity as well as multiple outflowing shell structures. We distinguish three different shells with constant expansion ($\sim$4–6 km s^{-1}) and possible rotation signatures ($\leqslant$0.5 km s^{-1}). We find that the shells can be explained by magnetocentrifugal disk winds with launching radii $R_{\rm launch} \lesssim 4$ au and a small magnetic lever arm $\lambda \sim 1.6$–1.9. The multiple shell structure may be the result of episodic ejections of the material from the accretion disk associated with three different epochs with dynamical ages of 497 ± 15 yr, 310 ± 9 yr, and 262 ± 11 yr for the first, second, and third shells, respectively. The outermost shell was ejected 187 ± 17 yr before the middle shell, while the middle shell was launched 48 ± 14 yr before the innermost shell. Our estimations of the linear and angular momentum rates of the outflow as well as the accretion luminosity are consistent with the values expected if the outflow of HH 30 is produced by a wide-angle disk wind.

Unified Astronomy Thesaurus concepts: Accretion (14); Herbig-Haro objects (722); Star formation (1569); Stellar winds (1636); Young stellar objects (1834)

1. Introduction

Molecular outflows and protostellar jets are phenomena present in the star formation process. However, the link between these flows and the connection with the protostar–disk system are still open questions. These flows play an important role in the evolution of the protostar–disk system because they could be responsible for extracting the excess of angular momentum and could limit the mass from the protostar–disk system (Blandford & Payne 1982; Shu et al. 1993).

The protostellar jets are explained as winds ejected directly from inner regions of the accretion disk, very close to the central protostar, by the magnetocentrifugal mechanism, where the magnetic field anchored to the accretion disk drives and collimates them (see reviews by Konigl & Pudritz 2000; Shu et al. 2000). The molecular outflows are interpreted in two different ways: as swept-up material or as material directly ejected from the disk. In the former interpretation, the swept-up gas traces the interaction between the protostellar jet (or a slow disk wind) and the infalling envelope or parent core (Zhang et al. 2016). This interpretation has been used to explain Class 0 and I systems (e.g., Lee et al. 2000), as well as very massive molecular outflows (e.g., Zapata et al. 2015; López-Vázquez et al. 2019, 2020). In the alternative explanation, the molecular outflows comprise material directly from the accretion disk (e.g., Pudritz & Norman 1986). This interpretation can explain the rotation signatures found in several sources, such as CB 26 (Launhardt et al. 2009; López-Vázquez et al. 2023), Ori-S6 (Zapata et al. 2010), HH 797 (Pech et al. 2012), TMC1A (Bjerkeli et al. 2016), Orion Source I (Hirota et al. 2017), HH 212 (Lee et al. 2018), HH 30 (Louvet et al. 2018), NGC 1333 IRAS 4C (Zhang et al. 2018), DG Tau B (de Valon et al. 2020, 2022), and HD 163296 (Booth et al. 2021).

For the very massive molecular outflows associated with DG Tau B (Zapata et al. 2015) and Orion Source I (López-Vázquez et al. 2020), the authors showed that the slow disk winds ejected directly from the accretion disk do not have enough mass to account for the observed linear and angular momentum rates of these outflows. Their argument is based on the assumption that the mass-loss rate of the wind is a small fraction of the mass accretion rate of the disk. Therefore, these large masses of molecular outflows could be explained if the outflow is formed by entrained material from the parent cloud. Nevertheless, the estimated rates at millimeter wavelengths are a lower limit. For more realistic estimates of the mass-loss rate and the linear and angular momentum rates, it is necessary to consider the emission of the different atomic and molecular lines of the bipolar outflow detected at optical and near-infrared wavelengths, as shown in several sources such as HH 211 (Ray et al. 2023), and B335, HOPS153, HOPS370, IRAS16253, and IRAS20126 (Federman et al. 2023). For the case of DG Tau B, the linear momentum rate of the outflow is similar to the rate measured in the high-velocity atomic jet (Mitchell et al. 1994;

[7] Corresponding author.

Podio et al. 2011), although, if we consider the contribution of the jet, the large discrepancy between the rates is not explained. Recent nonideal magnetohydrodynamic simulations of the disk wind show that this fraction could be large enough to explain large masses (e.g., Bai & Stone 2017; Wang et al. 2019). Also, the abundances of the molecules used for the mass estimation can vary by one or two orders of magnitude (Wright et al. 2022), hence the H_2 mass in these outflows could be much lower than estimated from the outflows of DG Tau B and Orion Source I. However, both mechanisms may act simultaneously and the jet and wide-angle wind could coexist.

The ratio of the mass-loss rate to the accretion rate is thought to be around ∼10% (Ellerbroek et al. 2013), although recent studies have shown that this ratio can be around ∼50% (Lee 2020; Podio et al. 2021). However, for many sources a constant accretion rate implies that the source does not reach the final mass consistent with the initial mass function (Evans et al. 2009; Caratti o Garatti et al. 2012). This scenario may suggest that the accretion may be episodic (Frank et al. 2014). The greatest evidence for episodic ejections from the accretion disk has been observed in jets that show a series of knots along their axes, such as HH 211 (Lee et al. 2007), CARMA-7 (Plunkett et al. 2015), and HH 212 (Lee et al. 2017). Through recent high-resolution Atacama Large Millimeter/submillimeter Array (ALMA) observations, the evidence for episodic ejections has been reported from the molecular outflows HH 46/47 (Zhang et al. 2019), DO Tauri (Fernández-López et al. 2020), and DG Tau B (de Valon et al. 2022), in which the authors show that the molecular outflow has an internal multiple shell structure, where the outer shell could be associated with the material swept up by the disk wind, while the internal shells are associated with a short episodic wind or jet outburst ejected directly from the accretion disk every few hundred years.

Located in the dark cloud L1551 at a distance of $\sim 141 \pm 7$ pc (Zucker et al. 2019) in Taurus, HH 30 is a young molecular outflow associated with a T Tauri star with an enclosed mass of $0.45 \pm 0.04\ M_{\odot}$ and a spectral class M0 ± 1 (Pety et al. 2006); the central source has a bolometric luminosity of 0.2–0.9 $L_{\odot}$ (Cotera et al. 2001) and a velocity $V_{\rm lsr} = 6.9 \pm 0.1$ km s^{-1} (Louvet et al. 2018). The HH 30 system is a typical protostellar object with an edge-on accretion disk with a mass of dust of $>25.5\ M_{\oplus}$ (Villenave et al. 2020). The ballistic jet of HH 30 has a size of 7′ and presents wiggling and orbital motions of the central star in a binary system with a period <1 yr (Anglada et al. 2007), and a large-scale C-shape due to proper motion of the system or due to the action of winds from other stars (Estalella et al. 2012). Whereas the optical jet is bipolar, the outflow is only seen north of the disk and constitutes an example of a monopolar outflow (e.g., Fernández-López et al. 2013), possibly due to the lack of molecular material south of the disk; that is, HH 30 may be located at the boundary of the parental core (Stanke et al. 2022). In previous work, Louvet et al. (2018) focused on studying a region of the HH 30 outflow near to the central protostar (i.e., at heights lower than $z \sim 3\farcs0$). They found that the properties of the outflow can be explained by a slow disk wind.

Here we present ALMA observations of the emission of the molecular lines of ^{12}CO ($J = 2$–1) and ^{13}CO ($J = 2$–1) of the protostellar outflow and the accretion disk associated with HH 30. In this work, we analyze the morphology and the kinematics of the outflow at larger scales. The paper is organized as follows. Section 2 details the observations. The results are shown in Section 3 and discussed in Section 4. Finally, the conclusions are presented in Section 5.

2. Observations

The archival observations of HH 30 were carried out with ALMA in band 6 on 2015 July 19 and 21 as part of the program 2013.1.01175.S (P.I. Catherine Dougados) and in band 6 on 2018 October 21 and 22, and November 7 and 10, as part of the program 2018.1.01532.S (P.I. Fabien Louvet) at the phase center α (J2000) = $04^{\rm h}31^{\rm m}37\fs47$ and δ(J2000) = +18°12′24.″22.

The integration time on-source was about 106 minutes, and 34 minutes was used for calibration for the 2015 observations, while for the 2018 observations it was about 106 minutes on-source and 212 minutes for calibrations. For the 2015 observations, the ALMA digital correlator was configured with five spectral windows centered on 230.546 GHz (spw0), 234 GHz (spw1), 220.379 GHz (spw2), 219.562 (spw3), and 217.052 GHz (spw4), with 960 channels and a spectral resolution of 122 kHz or about 0.17 km s^{-1} for spw0, spw2, and spw3, and with 128 channels and a space channel of 15.625 MHz or about 21.5 km s^{-1} for the continuum spectral windows (spw1 and spw4). For the 2018 observations the correlator was configured with six spectral windows centered on 233.994 GHz (spw0), 231.214 GHz (spw1), 230.531 GHz (spw2), 216.994 GHz (spw3), 220.393 GHz (spw4), and 219.554 GHz (spw5). The spectral windows spw1, spw2, spw4, and spw5 have 480 channels of 122 kHz or about 0.17 km s^{-1}, while the continuum spectral windows (spw0 and spw3) have 64 channels of 31.250 MHz width or about 40.19 km s^{-1} and 960 channels of 1.953 MHz or 2.69 km s^{-1}. The spectral lines reported in this study were found in spw0 (^{12}CO) and spw2 (^{13}CO) for 2015 observations and in spw2 (^{12}CO) and spw4 (^{13}CO) for 2018 observations.

For both sets of observations, the weather conditions were reasonably good and stable with a mean value of the precipitable water vapor (PWV) ≈0.9 mm for these high frequencies. The observations used the quasars J0423–0120, J0423–013, J0522–3627, J0510 + 1800, and J0502 + 1338 for calibration of amplitude, phase, bandpass, pointing, water vapor radiometer, and atmosphere.

The data were calibrated using the common astronomy software application (CASA) package (CASA Team et al. 2022) version 4.3.1 and version 5.4.0 for the projects 2013.1.01175.S and 2018.1.01532.S, respectively. After calibration the data were self-calibrated. We combined the data from the two observation programs and produced images using a robust parameter of 0.5. The final velocity cubes have rms noise levels of 1.07 and 0.96 mJy beam^{-1} for ^{13}CO and ^{12}CO data respectively. Finally the angular resolutions are $0\farcs32 \times 0\farcs26$ with a position angle (PA) of $-6\fdg91$ and $0\farcs32 \times 0\farcs27$ with a PA of $-5\fdg93$, for the ^{13}CO and the ^{12}CO cubes, respectively.

3. Results

3.1. Disk Emission

Figure 1 shows ^{13}CO molecular line emission from the disk associated with the HH 30 system. The color map of Figure 1(a) presents the first moment or the intensity-weighted velocity map overlaid in black contours by the moment-zero map. The east side of the disk has blueshifted velocities, while

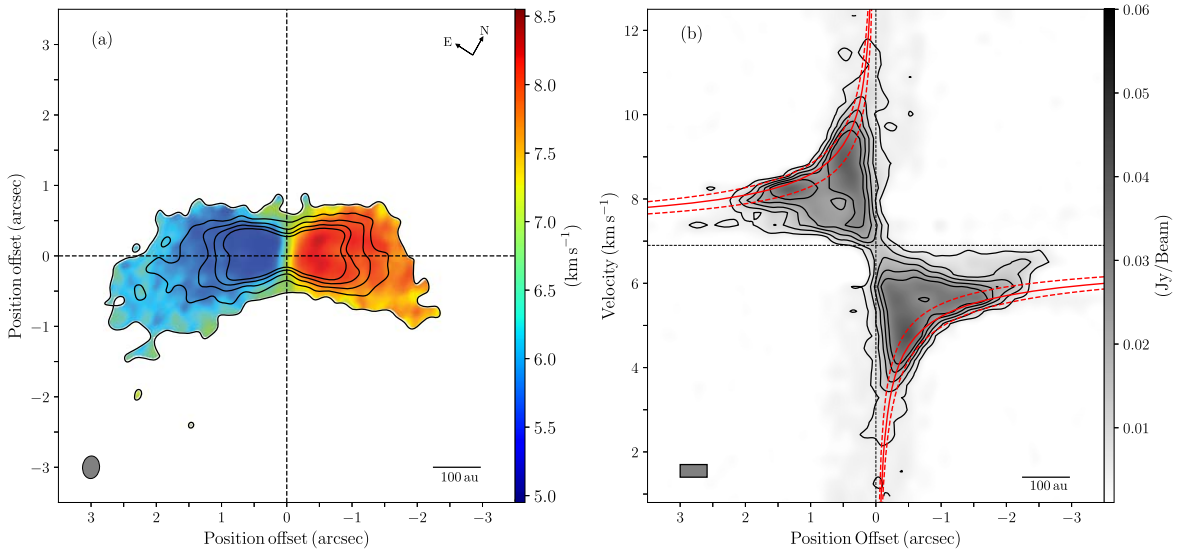

Figure 1. HH 30 disk emission of the ^{13}CO ($J = 2$–1) molecular line. (a) ALMA first moment or the intensity-weighted velocity of the accretion disk overlaid by contours of the moment zero (integrated intensity). Contour levels start from 5σ with steps of 5σ, 10σ, 15σ, and 20σ, where $\sigma = 2.13 \times 10^{-3}$ Jy beam^{-1} km s^{-1}. The synthesized beam of the disk image is shown in the lower left corner of the panel. The moments were integrated over a range of velocities from 3 to 11 km s^{-1}. (b) Position–velocity diagram over the disk midplane (horizontal black dashed line in panel (a)). The red solid lines show a Keplerian velocity profile surrounding the 0.45 $M_\odot$ central object, while the red dashed lines represent Keplerian velocity profiles corresponding to 0.31 $M_\odot$ and 0.59 $M_\odot$ (inner and outer curves, respectively). The gray bar represents the angular resolution (0.″3 or 42 au) and the channel width (0.3 km s^{-1}). Contour levels start from 5σ with steps of 5σ, 10σ, 15σ, and 20σ, where $\sigma = 1.07 \times 10^{-3}$ Jy beam^{-1}.

the west side presents redshifted velocities. This difference in velocities is evidence of the rotation of the disk.

Figure 1(b) is the position–velocity diagram along the disk midplane. The fits correspond to Keplerian curves $v_k = \sqrt{GM_{\rm dyn}/r}$, where G is the gravitational constant and r is the radius. In order to get the best fit, we used the pvanalysis package of the Spectral Line Analysis/Modeling (SLAM) code (Aso & Sai 2023). The pvanalysis tool extracts rotation curves based on the methods using the edge (Seifried et al. 2016) and ridge (e.g., Aso et al. 2015; Sai et al. 2020) of the emission in the position–velocity diagram. The red solid lines correspond to a dynamical mass of $M_{\rm dyn} = 0.45 \pm 0.14\,M_\odot$. This value is the best fit of the average of the dynamical masses obtained using the peaks of the emission $M_{\rm dyn} = 0.31\,M_\odot$ (inner dashed lines) and the 5σ limit of the emission $M_{\rm dyn} = 0.59\,M_\odot$ (outer dashed lines); the dynamical mass obtained with the average of the best fits matches the value previously reported by Pety et al. (2006).

3.2. Molecular Outflow Emission

The emission of the ^{12}CO in the molecular outflow associated with HH 30 is shown in Figure 2; the images of this figure are rotated by an angle of 31°.6, the orientation of the jet axis (Anglada et al. 2007). Figure 2(a) shows the ALMA moment zero; the emission of the outflow extends up to $\sim$19″. The black dots denoted by $A_{1,2,3}$, $B_{1,2,3}$, and C correspond to the [S$_{\rm II}$] jet knots reported by Anglada et al. (2007); the positions of the jet knots are corrected by the proper motions measured by Estalella et al. (2012) and considering a position offset corresponding to 8 yr, which is the difference between their observations made in 2010 and the observations reported in this work made in 2018. The ALMA first moment of the outflow is presented in Figure 2(b) where the molecular outflow presents signatures consistent with rotation of the gas at heights $z \leqslant 4''$, and the rotation velocity is $\lesssim$0.5 km s^{-1}. In this region, the outflow has blueshifted velocities on the east side and redshifted velocities on the west side. For very low heights $z < 1''$, the rotation of the gas is dominated by the accretion disk. The high velocity observed (>8 km s^{-1}) at a height $4'' < z < 6''$ of the gas, between knots A_1 and A_2, could be associated with entrained material from these knots. Figure 2(c) shows the dispersion velocity or moment-two map. The inner part of the outflow presents larger velocity dispersion than the walls, this effect may be due to the interaction of the innermost high-velocity jet (the jet seen at optical wavelengths) with the molecular environment or the material from wide-angle wind. The fact that in panel (c) we do not observe the high velocity presented in panel (b) at a height $4'' < z < 6''$ could be due to the dispersion velocity in this region is similar to the dispersion velocity caused by the high-velocity jet.

Figure 3 shows the ALMA moment-zero of the molecular outflow integrated over different velocity regimes. Figure 3(a) shows the moment zero integrated from −0.1 to 2.3 km s^{-1} and from 11.3 to 14 km s^{-1}. These ranges correspond to high velocities with respect to the velocity $V_{\rm lsr} = 6.9 \pm 0.1$ km s^{-1}. This figure shows the emission of the outflow close to the accretion disk, while the walls of the cavity outflow (magenta line) are shown in Figure 3(b), where the moment zero is integrated over velocities close to $V_{\rm lsr}$, from 2.6 to 11 km s^{-1}. The full range of emission is presented in Figure 3(c). Finally, Figure 3(d) is the position–velocity diagram along the jet axis. This diagram shows a convex spur structure, which is the signature of the jet-driven bow shocks (Lee et al. 2001). These bow shocks could be associated with the S$_{\rm [II]}$ knots of Figure 2, but they are not detected with our observations. The position–velocity diagram may trace the walls of the molecular outflow, which tend to have a constant velocity. Also, this diagram shows a possible internal structure at a height $2'' \lesssim z \lesssim 5''$, which could be associated with gas at different velocities (8 km s^{-1} $\lesssim V \lesssim$ 14 km s^{-1}). The apparent lack of emission at velocities near $V_{\rm lsr}$ could be associated with absorption by a slightly colder component at $V = V_{\rm lsr}$ in front of HH 30.

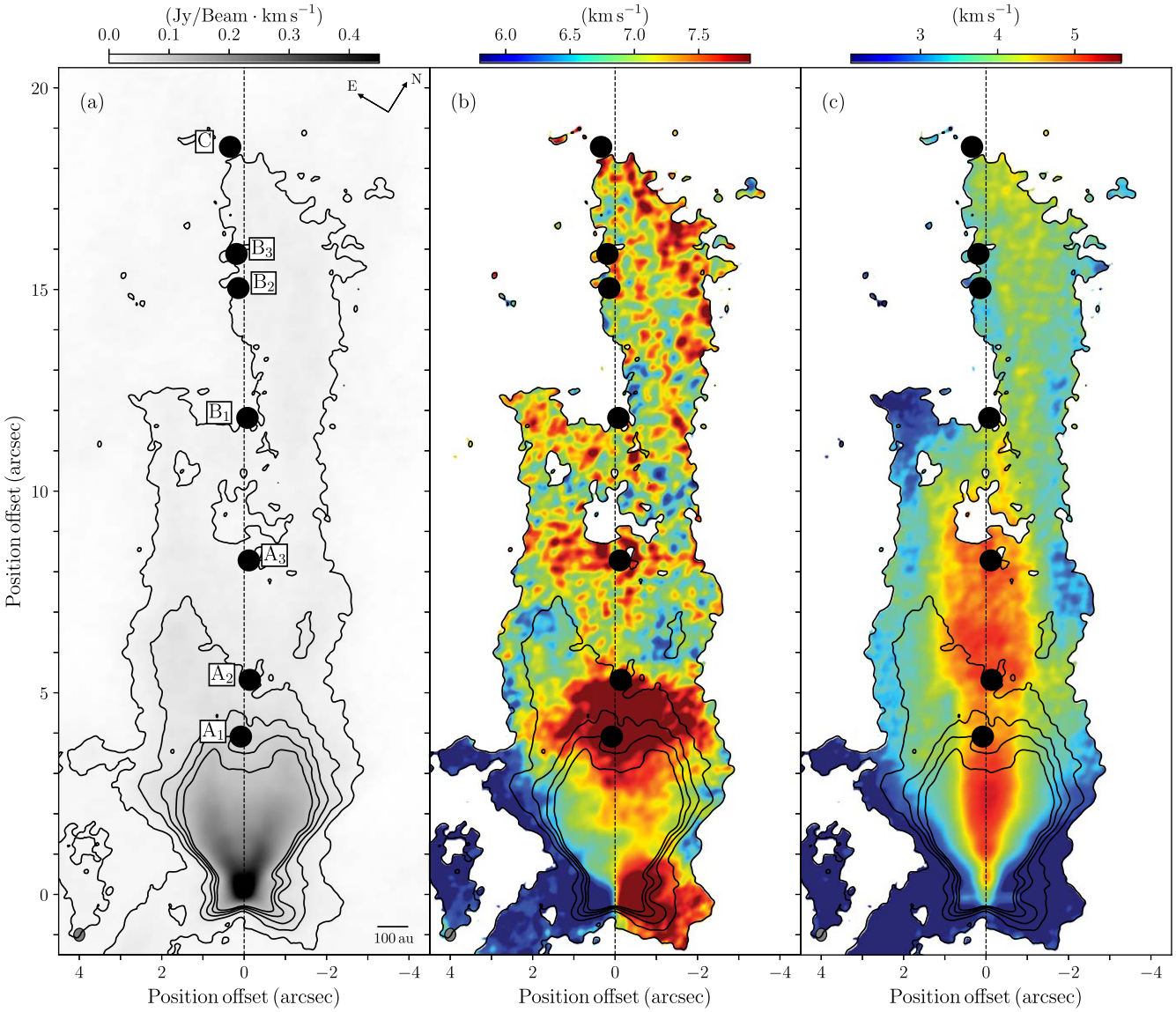

Figure 2. HH 30 molecular line emission from the ^{12}CO ($J = 2$–1) molecular line. (a) ALMA moment zero or integrated intensity. (b) ALMA first moment or the intensity-weighted velocity. (c) ALMA second moment or the intensity-weighted dispersion velocity. The black dots represent the [S$_{II}$] jet knots reported by Anglada et al. (2007) and Estalella et al. (2012). The knots in all panels are corrected by the proper motions. The synthesized beam is shown in the lower left corner. The contour levels in the three panels start from 3σ with steps of 3σ, 6σ, 9σ, and 12σ, where $\sigma = 6.69 \times 10^{-3}$ Jy Beam^{-1} km s^{-1}.

In addition, position–velocity diagrams perpendicular to the jet axis at different heights above the disk midplane were made. The left panel of Figure 4 shows, as an example, a position–velocity diagram at a height of $z = 3\farcs6$. The black dashed lines represent the jet axis (vertical line) and the velocity V_{lsr} (horizontal line). The solid red line is a vertical cut made to obtain the spectrum shown in the right panel of Figure 4. In the spectrum, five peaks can be observed, which may be correlated with the emission of three putative different shells. This cut is shown as an example to explain our method of detecting these shells. To ensure that the outflow has internal multiple shells, we selected different spectra to the one shown in the right panel of Figure 4.

Position–velocity diagrams perpendicular to the jet axis at different heights are shown in Figure 5. The diagrams were made from $z = 0\farcs3$ (or $\sim$42 au) to $z = 4\farcs8$ (or $\sim$672 au) every $0\farcs3$. At heights close to the accretion disk ($z \leqslant 1\farcs5$), we only detect one shell, while for intermediate heights ($1\farcs8 \leqslant z \leqslant 2\farcs7$), we can distinguish two shells. Finally, for great heights ($z \geqslant 3\farcs0$), we detect three possible shells. In a previous work, Louvet et al. (2018) found an inner shell at a height of $z = 2\farcs25$, and we confirmed the presence of this shell with the observations reported in this work. Such shell structure is consistent with radially expanding shells or bubbles (Arce et al. 2011; Zapata et al. 2011, 2014) and is similar to the elliptical structure expected in position–velocity diagrams of an outflow with a low inclination angle with respect to the plane of the sky (Lee et al. 2000). We made cuts in each position–velocity diagram at different positions every $0\farcs15$ and extracted the spectra from each of these cuts. We made a Gaussian fit to the spectra and identified peaks and correlated them with a structure in position, defining a new point in the position–velocity diagram with its error bar. We fit ellipses to the points associated with the peaks of the spectra assuming that these points trace a single structure. The fitted ellipses are obtained using the lsq-ellipse package from Python. We have numbered these shells 1, 2, and 3 for the red, blue, and green

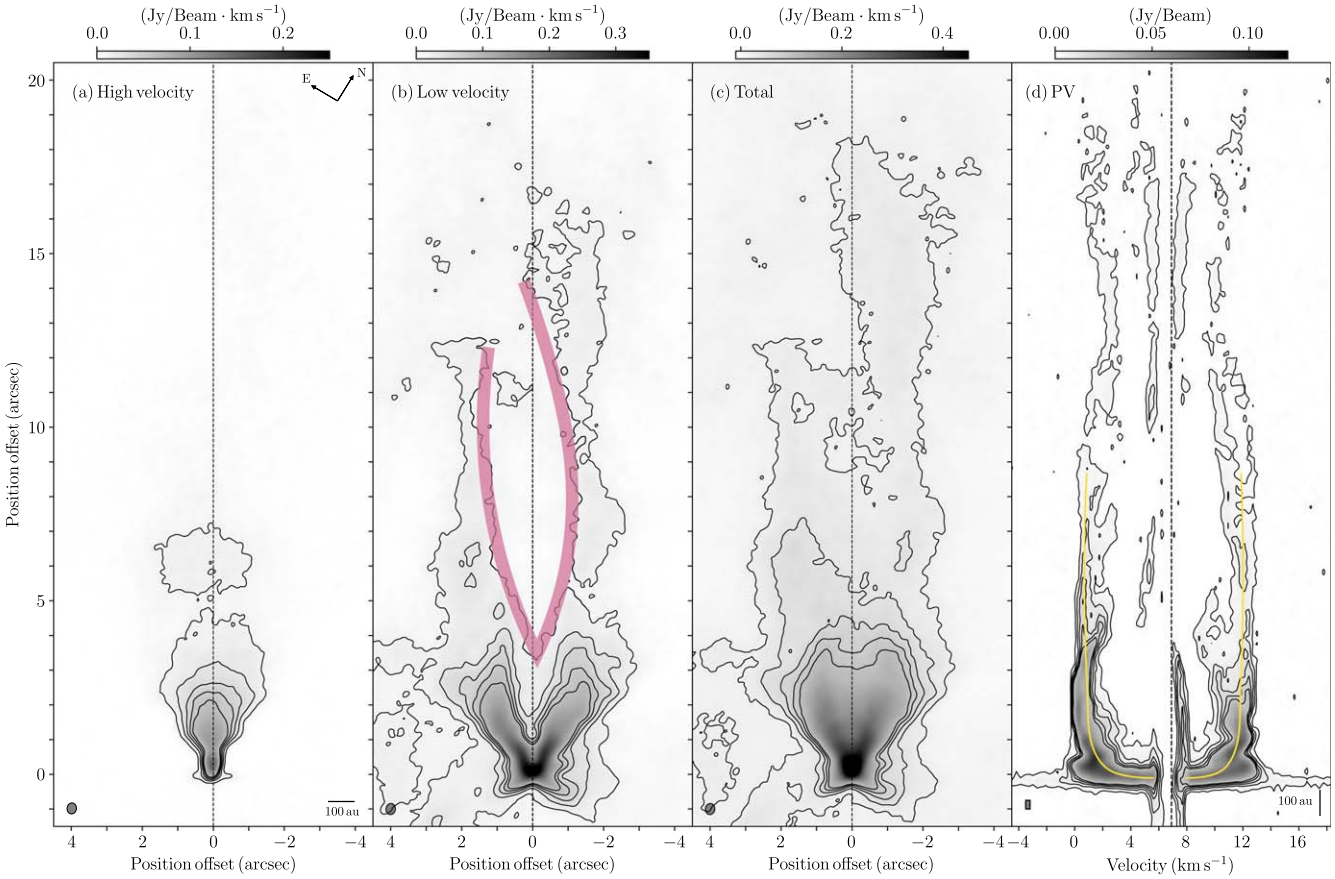

Figure 3. ALMA moment zero of the molecular outflow associated with HH 30 integrated over different ranges of the line-of-sight velocity. (a) High velocities, from −0.1 to 2.3 km s^{-1} and from 11.3 to 14 km s^{-1}. (b) Low velocities, from 2.6 to 11 km s^{-1}. (c) Full range of the emission, from −0.1 km s^{-1} to 14 km s^{-1}. (d) Position–velocity diagram along the jet axis. The synthesized beam of panels (a), (b), and (c) is shown in the lower left corner. The magenta line in panel (b) traces an internal cavity of the molecular outflow. The yellow lines in panel (d) indicate the convex spur structure, and the gray bar represents the angular resolution (0.″3 or 42 au) and the channel width (0.3 km s^{-1}) used for the position–velocity cut. The contour levels in panels (a)–(c) start from 3σ with steps of 3σ, 6σ, 9σ, and 12σ, where (a) $\sigma = 3.69 \times 10^{-3}$ Jy beam^{-1} km s^{-1}, (b) $\sigma = 3.93 \times 10^{-3}$ Jy beam^{-1} km s^{-1}, and (c) $\sigma = 5.87 \times 10^{-3}$ Jy beam^{-1} km s^{-1}. The contour levels in panel (d) start from 3σ with steps of 6σ, 12σ, 18σ, and 24σ, where $\sigma = 9.62 \times 10^{-4}$ Jy beam^{-1}.

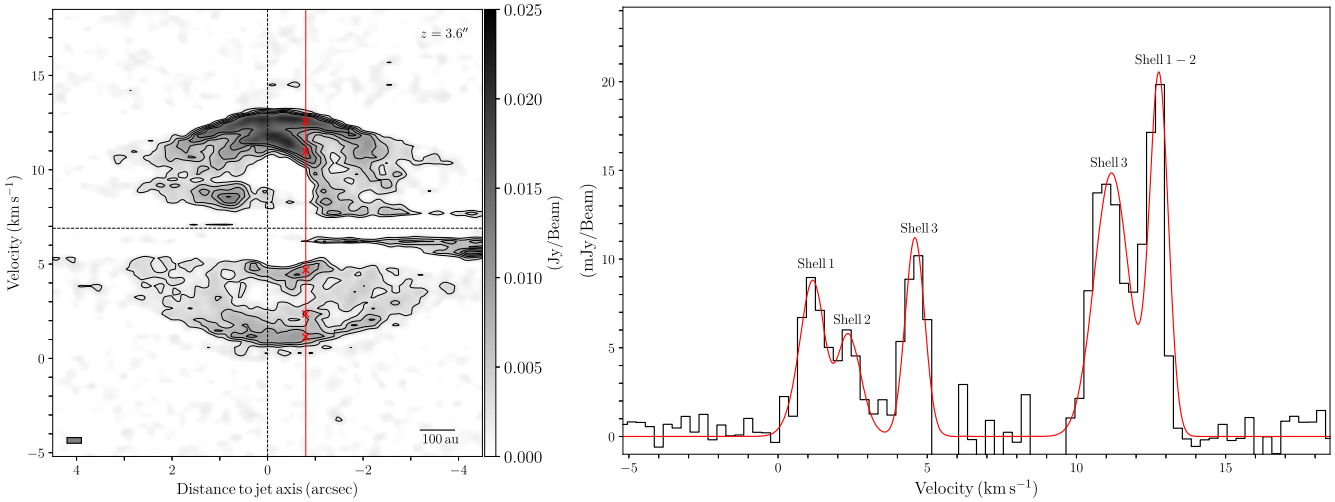

Figure 4. Left panel: position–velocity diagram perpendicular to the jet axis at a height of $z = 3.''6$ above the disk midplane. The contours start from 3σ with steps of 3σ, 6σ, 9σ, and 12σ, where $\sigma = 0.96 \times 10^{-3}$ Jy beam^{-1}. The vertical dashed line represents the position of the jet axis, while the horizontal line shows $V_{\rm lsr} = 6.9$ km s^{-1}. The gray bar represents the angular resolution (0.″3 or 42 au) and the channel width (0.3 km s^{-1}). The red line denotes a vertical cut along which the spectrum of the right panel was obtained and the red crosses are the positions of the peaks of the emission. Right panel: spectrum obtained through the vertical cut of the position–velocity diagram of the left panel. The black solid line represents the emission observed and the red solid line is the best five-Gaussian fit.

ellipses, respectively. As mentioned above, the elliptical shape of the three shells is evidence that they are in radial expansion, and the expansion velocity does not vary with distance to the protostar. The inclination of the shells with respect to jet axis (vertical dashed lines) is evidence of rotation. The signature of rotation is more evident in shells 2 and 3.

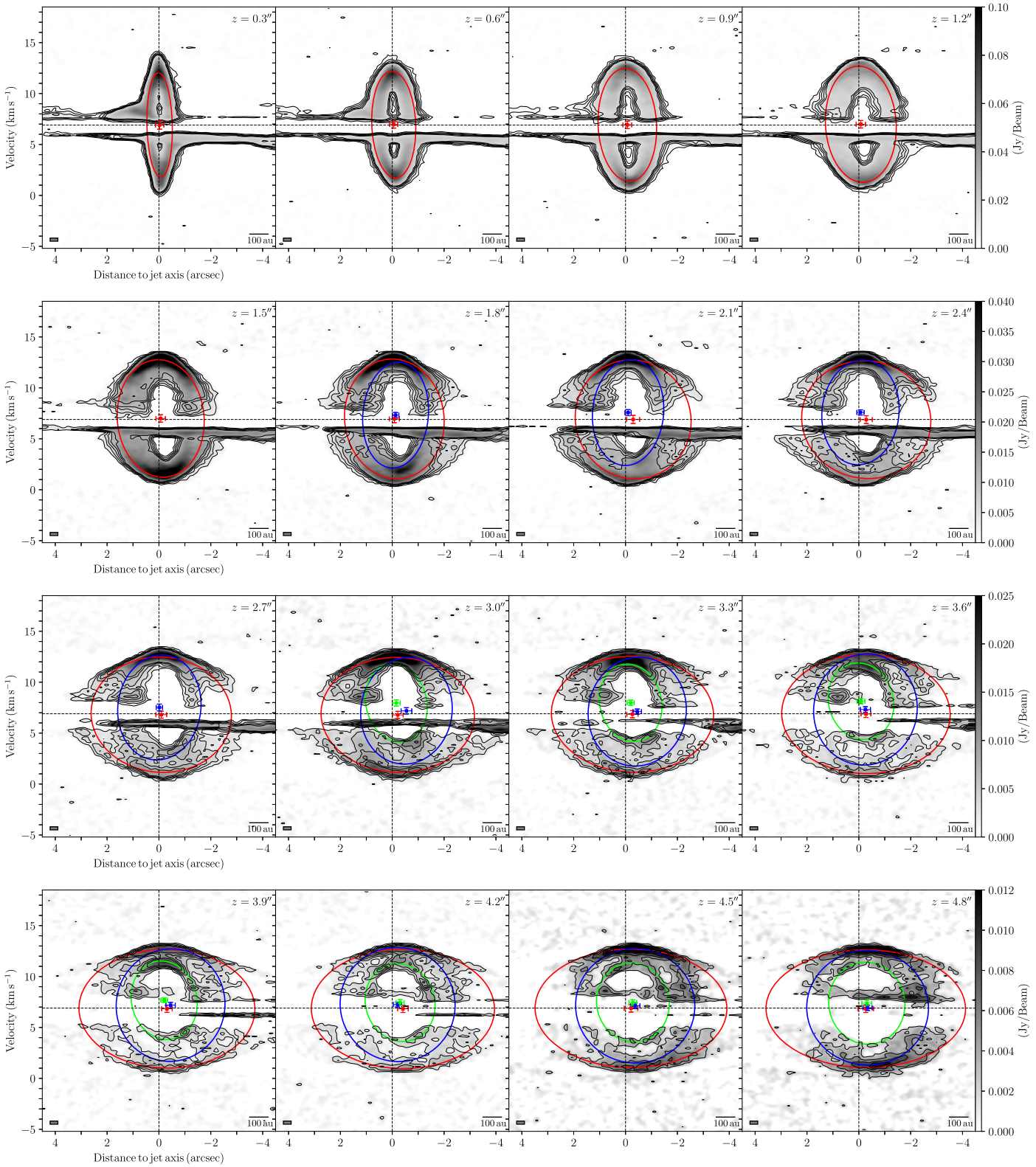

Figure 5. Position–velocity diagrams from the ^{12}CO emission perpendicular to the jet axis at different heights from $z = 0\farcs3$ (42 au) to $4\farcs8$ (672 au) at intervals of $0\farcs3$ (42 au). The gray bar represents the angular resolution ($0\farcs3$ or 42 au) and the channel width (0.3 km s^{-1}). The ellipses in the different panels represent the best fit for shell 1 (red), shell 2 (blue), and shell 3 (green), and the crosses show the center of each ellipse. The contour levels start from 3σ with steps of 3σ, 6σ, 9σ, and 12σ, where $\sigma = 0.96 \times 10^{-3}$ Jy beam^{-1}. The vertical dashed line represents the position of the jet axis, while the horizontal line shows $V_{\rm lsr} = 6.9$ km s^{-1}.

3.3. Kinematic and Physical Properties of the Molecular Outflow

To determine the kinematic and physical properties of the molecular outflow, we use the outflow model presented by Louvet et al. (2018; hereafter Louvet's model). In this model, they consider that for each height z the ^{12}CO emission arises from a narrow circular ring of gas. Louvet's model relates the physical properties of the circular ring, such as the radius R, the

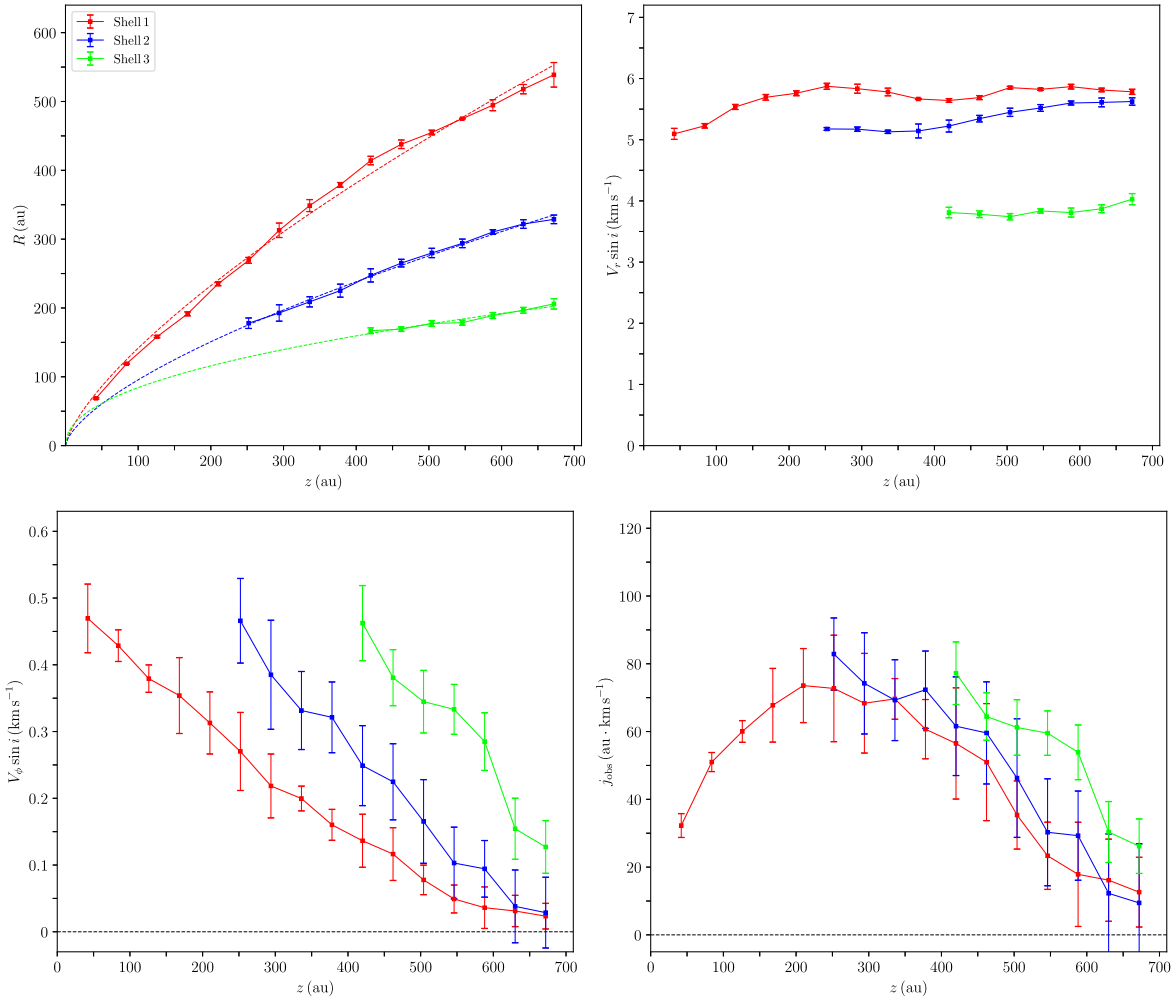

Figure 6. The kinematic properties of the HH 30 molecular outflow for the different shells as a function of height z. Top left: the cylindrical radius. Top right: the expansion velocity perpendicular to the jet axis. Bottom left: the rotation velocity. Bottom right: the specific angular momentum. The error bars are derived from the Gaussian fit (see text). The dotted lines in the top left panel correspond to the best fitting of the general relation $z = aR^{-\beta/2}$ where the values of a and β for each shell are shown in the text.

center $x_{\rm offset}$, and the velocity field (V_r, V_z, and V_ϕ), with the parameters of an ellipse, PA, major a and minor b axes, and the center coordinates ($r_{\rm cent}$ and $V_{\rm cent}$). This model considers the wiggling movements and the inclination angle with respect to the line of sight i. The equations of Louvet's model are

$$x_{\rm offset} = r_{\rm cent}, \tag{1}$$

$$V_z = -(V_{\rm cent} - V_0)/\cos i, \tag{2}$$

$$(V_r \sin i)^2 = ((\cos{\rm PA})^2/a^2 + (\sin{\rm PA})^2/b^2)^{-1}, \tag{3}$$

$$(V_\phi \sin i)/R = 0.5 \times (V_r \sin i)^2 \times \sin 2{\rm PA} \times (1/b^2 - 1/a^2), \tag{4}$$

$$1/R^2 = (\cos{\rm PA})^2/b^2 + (\sin{\rm PA})^2/a^2 - (V_\phi/R)^2/V_r^2, \tag{5}$$

where we can consider that $x_{\rm offset}$ is the distance between the horizontal center coordinate of the ellipse and the jet axis, and $V_{\rm cent}$ is the velocity offset between the vertical center coordinate and $V_{\rm lsr}$. Finally, V_0 is the projected cut velocity along the line of sight. In this case, $V_0 = 0$ km s^{-1} because we assume that the outflow is not wiggling.

The fitted ellipses of Figure 5 for shells 1, 2, and 3 are used to determine the kinematic properties shown in Figure 6. The top left panel presents the cylindrical radius as a function of the height for the three shells. These radii follow the general relation $z = aR^{-\beta/2}$, where the values of a and β for the best fit are $a = 1.29$, 0.85, and 0.70, and $\beta = -1.43$, -1.32, and -0.92, for shells 1, 2, and 3, respectively. The top right panel of Figure 6 plots the expansion velocity along the line of sight ($V_r \sin i$) as a function of the height. While shells 1 and 2 reach a constant value of $\sim$6 km s^{-1}, shell 3 presents constant velocity of $\sim$4 km s^{-1}. The rotation velocity along the line of sight ($V_\phi \sin i$) is shown in the bottom left panel. For all shells, the rotation velocity decreases with height. This behavior is observed in several sources, e.g., Orion Source I (Hirota et al. 2017; López-Vázquez et al. 2020), HH 212 (Lee et al. 2018), NGC 1333 IRAS 4C (Zhang et al. 2018), and CB 26 (López-Vázquez et al. 2023; Launhardt et al. 2023). It can be observed that shell 1 has the lowest rotation velocity while shells 2 and 3 have the highest. This behavior could be explained if the shells are associated with magnetocentrifugal disk winds; under this assumption, shell 3 is launching from the innermost region of the accretion disk and shell 1 is launched from the most extended region. Finally, the bottom right panel of Figure 6 shows the specific angular momentum $j_{\rm obs} = R \times V_\phi \sin i$. The specific

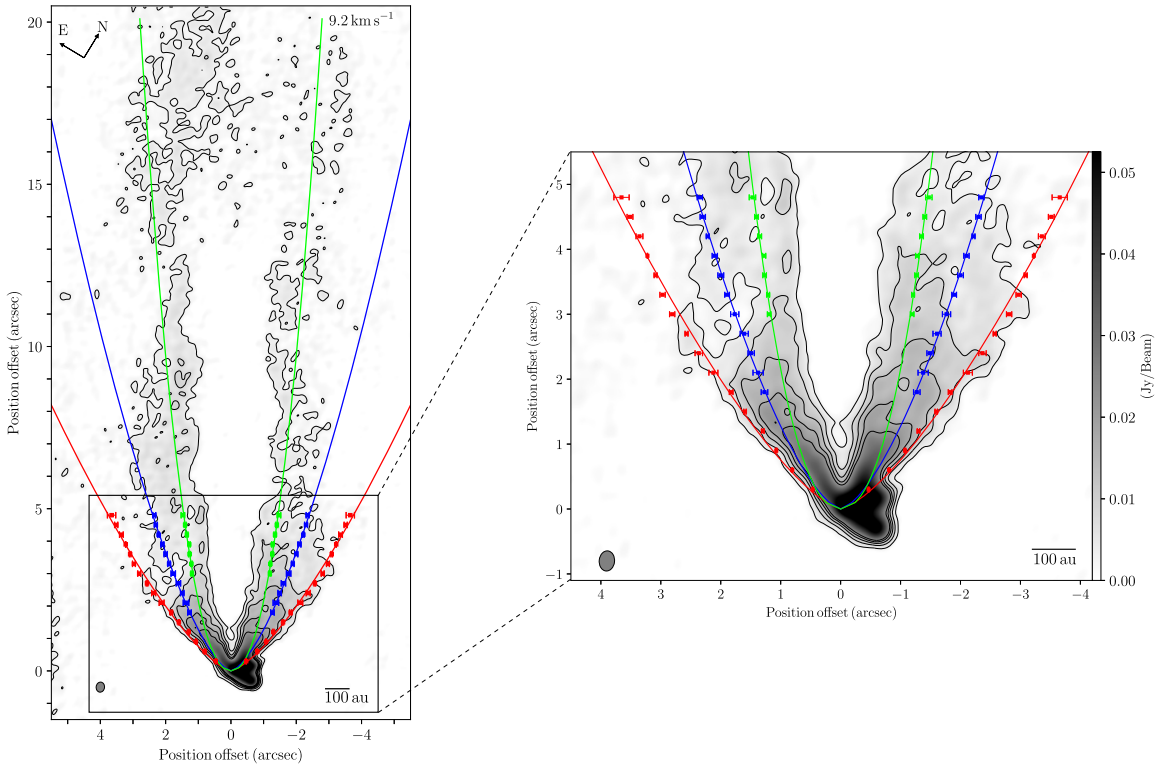

Figure 7. The ^{12}CO molecular line emission of the velocity channel of 9.2 km s^{-1} of the molecular outflow associated with HH 30. Left panel: all the detected outflow emission. Right panel: zoom into the central region. The solid lines and points show the position of the different shells: shell 1 (red lines), shell 2 (blue lines), and shell 3 (green lines). The synthesized beam in each panel is shown in the lower left corner. The contour levels start from 3σ with steps of 3σ, 6σ, 9σ, 12σ, and 15σ, where $\sigma = 0.96 \times 10^{-3}$ Jy beam^{-1}.

angular momentum has the same behavior as the rotation velocity, which decreases with height. Shells 2 and 3 seem to have more angular momentum than shell 1; however, if we consider the error bars in our estimations, we can conclude that the three shells at greater distances from the accretion disk ($z > 450$ au), statistically, have the same angular momentum. The error bars of these properties are derived through error propagation of the statistical uncertainties extracted in the ellipse fitting plugged into Equations (1)–(5).

The best fit of the general relation $z = aR^{-\beta/2}$ and the radius of the three shells are compared with measurements of the walls of the molecular outflow in one of the central channels, 9.2 km s^{-1}, which is shown in the left panel of Figure 7. The outflow cavity is observed with more detail in the central channels (close to $V_{\rm lsr} = 6.9 \pm 0.1$ km s^{-1}) shown in Figures 14 and 15 in the Appendix. The radii of shell 1 (red lines), shell 2 (blue lines), and shell 3 (green lines) trace the outflow cavity until a height of $z < 5''$, while shell 3 traces the outflow up to $z \sim 20''$. The fact that only shell 3 follows the outflow structure up to great heights could be because the other shells (1 and 2) are older than shell 3 and their greater expansion and cooling make them produce fainter CO emission; this effect is observed in perpendicular position–velocity diagrams presented in Figure 16 in the Appendix. The right panel of Figure 7 presents a zoom-in of the inner region of the outflow up to $z \lesssim 5''$, where our analysis was made.

For the heights considered in our analysis, the variation of the cylindrical radius with height can be approximated by a cone of semi-opening angle $\tan\theta = R/z$. We fitted these angles and obtain $46\overset{\circ}{.}0 \pm 0\overset{\circ}{.}1$, $30\overset{\circ}{.}0 \pm 0\overset{\circ}{.}3$, and $18\overset{\circ}{.}8 \pm 0\overset{\circ}{.}2$ for shells 1, 2, and 3, respectively. If the inclination of the cone axis with respect to the line of sight is the same as the inclination of the jet axis, the ratio of the projected velocity components is $V_r \sin i / V_{\rm cent} = \tan\theta \times \tan i$. Under this assumption and for measurements of $V_r \sin i$ and $V_{\rm cent}$ at each height mentioned above, we estimated the average inclination angle of the jet axis as $87\overset{\circ}{.}7 \pm 0\overset{\circ}{.}3$.

The velocity V_z, by convention, is positive for an outward-directed velocity component along the z-axis. Once the inclination angle is estimated for the three different shells, we obtain V_z by employing Equation (2). The values of this velocity are shown in the left panel of Figure 8. These velocities tend to a constant value for shell 1, while showing a slight increase with height for shells 2 and 3. The highest V_z velocity is that of shell 3. We also define a poloidal velocity, $V_p = \sqrt{V_r^2 + V_z^2}$. As can be seen in the right panel of Figure 8, its dependence on height is similar to that of V_z.

A possible origin of the multiple shell structure is that these shells are launched at different radii from the accretion disk and are driven magnetocentrifugally. Under this scenario, we can estimate the launching radius $R_{\rm launch}$ of all shells for each height with Anderson's relation (Anderson et al. 2003) given by

$$\varpi_\infty v_{\phi,\infty}\Omega_0 - \frac{3}{2}(GM_*)^{2/3}\Omega_0^{2/3} - \frac{v_{\rm p,\infty}^2 + v_{\phi,\infty}^2}{2} \approx 0, \qquad (6)$$

where ϖ_∞ is the distance between the jet axis and the cavity of the molecular outflow, which in our case is determined by the

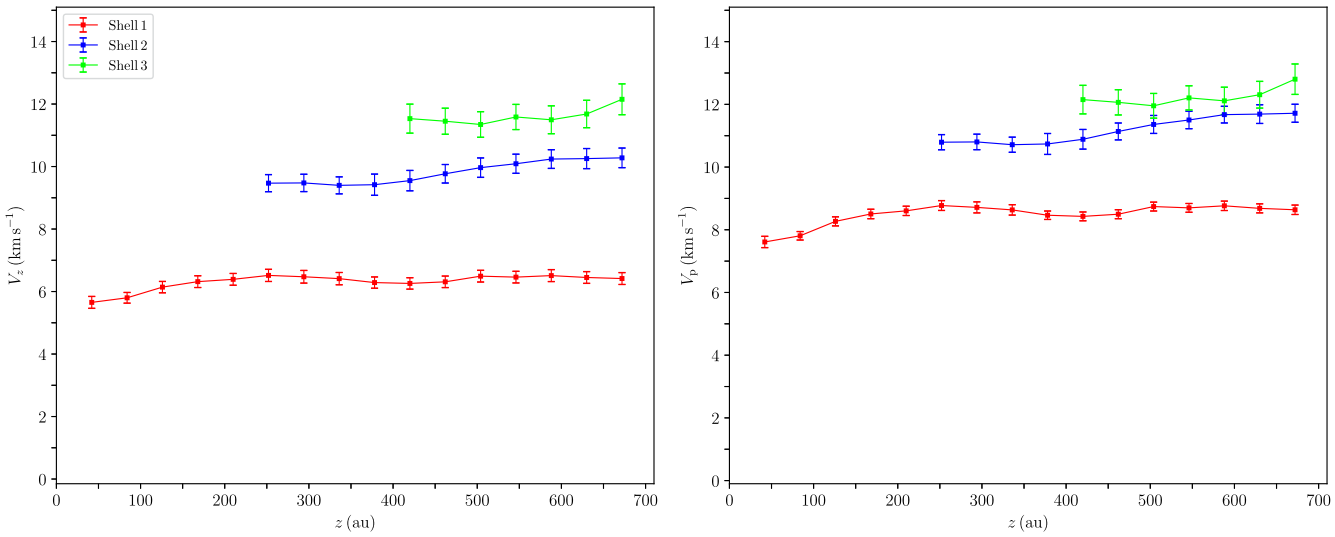

Figure 8. Left panel: The outward velocity V_z as a function of the height. Right panel: poloidal velocity ($V_p = \sqrt{V_r^2 + V_z^2}$) as a function of height. The error bars are derived from the Gaussian fits.

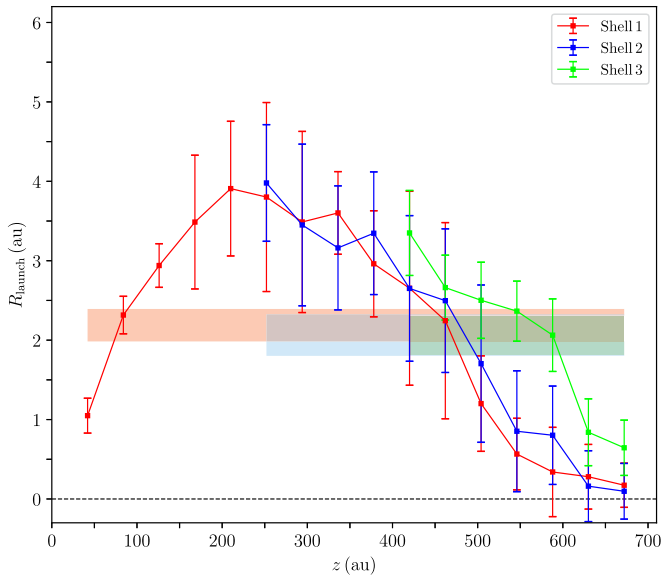

Figure 9. The launching radii as a function of height z. These radii are estimated by solving Anderson's relation (Anderson et al. 2003). The red, blue, and green rectangles are the mean launching radii for shell 1, 2, and 3, respectively. The error bars are derived from the Gaussian fit.

cylindrical radius for each height z. The velocities $v_{\phi,\infty}$ and $v_{\rm p,\infty}$ denote the toroidal and the poloidal velocities observed at cylindrical radii $V_\phi \sin i$ and V_p for this object. The variable G and M_* are the gravitational constant and the mass of the central protostar ($0.45 \pm 0.14\ M_\odot$). Finally, the variable Ω_0 is the angular speed $\Omega_0 = (GM_*/\varpi_0^3)^{1/2}$ at launching radius ϖ_0. The launching radii for the three different shells as a function of height are shown in Figure 9. The derived values of the launching radius are consistent with an outflow origin in the range $0.01\ {\rm au} < R_{\rm launch} < 4\ {\rm au}$ approximately. This range is consistent with that reported previously by Louvet et al. (2018). Our estimates for shell 1 present a peculiar behavior: close to the disk ($z \lesssim 200$ au) the launching radius increases with height, while at greater distances ($z \gtrsim 200$ au), it decreases with height. Shells 2 and 3 have the same behavior for large distances to the accretion disk, decreasing with height. This behavior could be because the rotation velocity and the specific angular momentum decrease with height as shown in different sources such as Orion Source I (Hirota et al. 2017), NGC 1333 IRAS 4C (Zhang et al. 2018), HH 212 (Lee et al. 2018), and CB 26 (López-Vázquez et al. 2023; Launhardt et al. 2023). However, if we take the mean value (the red, blue, and green rectangles of Figure 9), we find that the derived launching region is systematically the same for the three shells. Nevertheless, since the launching radii of the three shells are ∼0.01–4 au and they are spatially unresolved, we can summarize that the launching radii of the three shells can be expressed as 2 ± 2 au and we can assume that the three shells are launched from the same region.

3.4. Mass of the Outflow

Since the ^{13}CO is undetected below 3σ in the outflow (see also Louvet et al. 2018), we can assume that the ^{12}CO emission is optically thin. Hence, following the formalism in Zapata et al. (2014), we derive a lower limit for the mass of the molecular outflow using

$$\frac{M_{\rm H_2}}{M_\odot} = 1.2 \times 10^{-15} X_{\rm H_2/CO} \frac{\Delta\Omega}{\rm arcsec^2} \left(\frac{D}{\rm pc}\right)^2 \times \frac{\exp(5.53/T_{\rm ex})}{1 - \exp(-11.06/T_{\rm ex})} \frac{\int I_\nu\, dv}{\rm Jy\ km\ s^{-1}}, \quad (7)$$

where, we take $X_{\rm H_2/CO} = 10^{-4}$ for the fractional ^{12}CO abundance with respect to H_2, $\Delta\Omega$ is the solid angle of the source (138 arcsec^2), D is the distance (141 ± 7 pc), I_ν is the intensity of the emission in jansky, dv is the velocity range in km s^{-1}, and $T_{\rm ex}$ is the excitation temperature. For an excitation temperature of $T_{\rm ex} = 30$ K, and under the assumption that the emission is governed by a single excitation

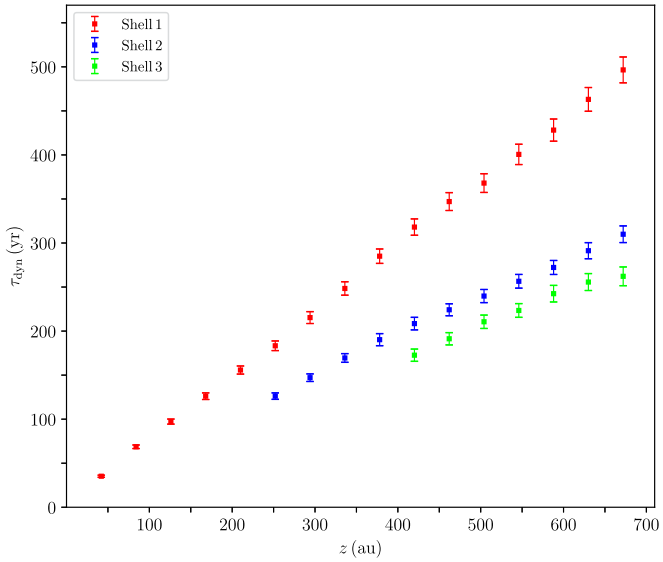

Figure 10. Dynamical time of the different shells of the molecular outflow HH 30 as a function of height z. The error bars are derived from the Gaussian fit.

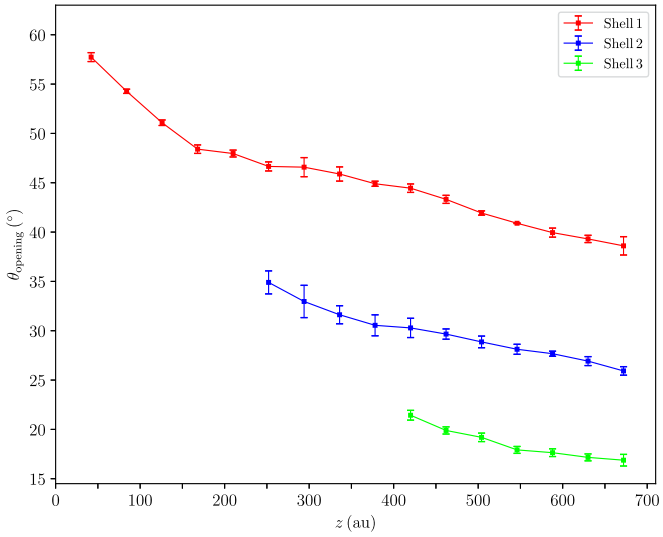

Figure 11. Opening angle of the different shells as a function of the height z. The error bars are derived from the Gaussian fit.

temperature (Louvet et al. 2018), the mass of the outflow is $M_{\rm outflow} = (1.83 \pm 0.19) \times 10^{-4}\ M_{\odot}$. This value is one order of magnitude bigger than reported by Louvet et al. (2018) and Pety et al. (2006). The main difference between our mass estimation and their reported mass is the sensitivity. Louvet et al. (2018) consider the emission of the source that exceeds 5σ with $\sigma = 3.6\ {\rm K\ km\ s^{-1}}$ and an angular size of $\sim$7.2 arcsec^2, while in this work we measured the emission that exceeds 3σ with $\sigma = 1\ {\rm K\ km\ s^{-1}}$ and an angular size of $\sim$138 arcsec^2.

4. Discussion

In this section, we present the different explanations for the multiple shell structure in the molecular outflow of HH 30, and we discuss the magnetocentrifugal process as a possible origin of the molecular outflow. Other possible scenarios such as photoevaporated disk winds and entrained material were addressed in the previous work by Louvet et al. (2018).

4.1. Origin of the Multiple Shell Structure

The emission from ^{12}CO shows that the molecular outflow associated with HH 30 presents an internal structure of multiple shells as shown in Figures 5 and 8 of Louvet et al. (2018). A similar internal structure of the molecular outflow has been reported in several sources such as HH 46/47 (Zhang et al. 2019), DO Tauri (Fernández-López et al. 2020), and DG Tau B (de Valon et al. 2022), where the authors interpreted that the presence of multiple shells in a molecular outflow is associated with episodic ejections of the material by a wide-angle wind from the accretion disk. To support the idea that the three shells found in the molecular outflow of HH 30 are associated with episodic ejections, we estimated their dynamical time as a function of height, $\tau_{\rm dyn} = z/V_z$. These results are presented in Figure 10. The shells reach their maximum height ($z_{\rm max} = 4\farcs8 \approx 672$ au) at $\sim 497 \pm 15$ yr, $\sim 310 \pm 9$ yr, and $\sim 262 \pm 11$ yr (shells 1, 2, and 3, respectively). Figure 10 shows that the difference in dynamical age between the first ejection (shell 1) and the second (shell 2) tends to a constant value of $\sim 187 \pm 17$ yr; the difference in dynamical age between the second ejection and the third (shell 3) has the same behavior with a value of $\sim 48 \pm 14$ yr.

We must consider that the estimated dynamical ages of these shells may not be their real ages since our estimation does not consider slowing-down effects due to the interaction with the surrounding material. Therefore, the dynamical ages of these shells are upper limits to their true age. Under this assumption, the intervals between the different episodic ejections are upper limits too. While these values are much higher than the kinematic ages of the knots $A_{1,2,3}$, $B_{1,2,3}$, and C of the HH 30 jet, they could be associated with the knots $E_{1,2,3b,4}$ located at a height $z > 35''$ with kinematic ages between 240.8 ± 1.7 yr and 413.7 ± 4.9 yr (Estalella et al. 2012). In this case, the ages of our shells 2 and 3 could be consistent with episodic outbursts in the collimated jet; however, the age of shell 1, $\sim$500 yr, makes it older than the E knots. This may be because the age of shell 1 is overestimated, or shell 1 could be associated with another episodic outburst that has not been observed. This suggests that the episodic nature seen in the jet and the outflow may originate from the same outburst event.

The opening angle of the molecular outflow can be an indicator of the evolution of these sources, that is, it increases with the source's age. Several studies (e.g., Arce & Sargent 2006; Seale & Looney 2008; Velusamy et al. 2014; Hsieh et al. 2017) have shown that this angle widens with time close to the source for different sources. To confirm this assertion, we estimate the opening angle as

$$\theta_{\rm opening} = \tan^{-1}\left(\frac{R - R_{\rm launch}}{z}\right) \approx \tan^{-1}\left(\frac{R}{z}\right). \quad (8)$$

The previous approximation takes into account that $R \gg R_{\rm launch}$. The difference between this angle and the semi-opening angle mentioned in Section 3.3 is that this angle is measured for all heights, while the semi-opening angle is a fit under the assumption that the material is following a cone structure. For the three shells, this angle has a maximum value close to the

midplane at a height of $z = 0\farcs3$, $\sim 57\fdg7 \pm 0\fdg5$ for shell 1, $\sim 34\fdg9 \pm 1\fdg2$ for shell 2, and $\sim 21\fdg4 \pm 0\fdg5$ for shell 3 as shown in Figure 11. In general, the opening angle will be increasing with time; therefore, the fact that shell 1 presents the largest opening angle is an indicator that this shell is the oldest, and shell 3, with the smallest opening angle, is the youngest. These values and this behavior are consistent with shells produced by episodic ejections.

Shang et al. (2023), through numerical simulations of X-wind outflows, present an alternative explanation for the observed shape of the ^{12}CO emission of the position–velocity diagrams presented in Figure 5. Their model considers that the molecular outflow is a result of the interaction between a wide-angle toroidally magnetized wind and magnetized isothermal toroids that represent molecular cloud cores before the onset of dynamical collapse. Under this assumption, shear, Kelvin–Helmholtz instabilities, and pseudo-pulse effects[8] could be responsible for the nested shells observed in the position–velocity diagrams of the molecular outflow of HH 30 for heights $z \leqslant 1\farcs5$. However, provided that the shells are well defined at heights $z > 1\farcs5$, the idea that the multiple shell structure is associated with episodic ejections is strengthened. We may assume that the nondetection of the multiple shell structure at heights close to the disk midplane ($z \leqslant 1\farcs5$) could be explained in two different ways: first, the observations do not have enough angular resolution to distinguish the multiple shell structure; second, if we assume that shell 1 is the result of the interaction between the disk wind and its parent cloud, basically as a rotating cloud in gravitational collapse (Ulrich 1976), it will tend to stagnate at some point close to the disk midplane, because the Ulrich-like envelopes have a barrier of infinite density. This barrier would slow down the shells, allowing younger shells to catch older ones.

4.2. Origin of the Outflow

Figures 2 and 3 show the structure of the molecular outflow associated with HH 30. In both figures the southern part of the outflow has not been detected; this may be because the source is located immediately at the southern boundary of the parental core (e.g., Stanke et al. 2022), or this monopolar shape could be a consequence of possible deflection effects (e.g., Fernández-López et al. 2013). The origin of this asymmetry is discussed in detail in Louvet et al. (2018).

We estimated the launching radii of the three shells in Section 3.3 through Anderson's relation and we obtain from Figure 9 that these radii are in a range between 0.01 and 5 au. These values are consistent with the expectations for magnetocentrifugal winds of Class II sources (Pascucci et al. 2022). In particular, Anderson et al. (2003) assume that the disk winds are driven by magnetic forces with a large-scale poloidal magnetic field anchored in the disk. They also consider that these winds are dynamically cold (negligible enthalpy), axisymmetric, and in a steady state. Therefore, the rotation is governed by the magnetic forces. Hence, wide-angle winds rotate preserving the sense of rotation of the disk. In the case that these winds were counter-rotating (dynamically warm winds), the launching point could not be estimated using Anderson's relation (Tabone et al. 2020). The HH 30 outflow preserves the direction of the disk rotation, justifying the usage of Anderson's expression to estimate the footpoint of the different shells.

Figure 9 shows that the mean launching region of shells 1, 2, and 3 is systematically the same. The particular behavior of shell 1 (increases and decreases with height) could be explained if shell 1 is produced by the interaction of the wide-angle disk wind with the surrounding material (e.g., López-Vázquez et al. 2019). If this is the case, Anderson's relation might not be the best method to estimate the launching point, because this relation considers that the wind has not interacted with the surrounding environment or with itself.

On the other hand, the drastic decrease in the launching radius with the height presented in all shells could be associated with the following three features. (1) The poloidal velocity (Figure 8(b)) of the three shells tends to be constant; therefore, the launching radius depends only on the behavior of the specific angular momentum. Given that this quantity decreases with the height, the launching radius decreases too; however, this could be inconsistent with the behavior expected for a disk wind. Hence, this behavior could be an indicator that the two internal shells could be produced by the interaction of the disk wind with itself, and Anderson's relation, as with shell 1, is not the best method to estimate their launching radii. (2) Our three shells could be the result of multiple ejections at three different times but with different launching points associated with the location of the gaps in the accretion disk (e.g., Suriano et al. 2017, 2018, 2019). (3) Our measurements of the outward, expansion, and rotation velocities could be contaminated by the entrained material produced by the knots A_1 and A_2 of the protostellar jet (see Figure 2); therefore, our estimation of the launching radii for the shells around those knots is contaminated by this effect too. With our current resolution we cannot resolve the disk, and we cannot distinguish which effect dominates the behavior of the launching radii as a function of the height, but Anderson's relation could be a good approximation that the launching region of the three shells could be the same as shown in Figure 12.

The magnetocentrifugal disk winds remove mass and angular momentum from the accretion disk and exert a torque on the disk surface (e.g., Pudritz et al. 2007; Alexander et al. 2014; Pascucci et al. 2022). An important parameter for describing the magnetic torque is the magnetic lever arm $\lambda = (r_A/r_0)^2$, where r_A is the cylindrical radius at the Alfvén surface and r_0 is the launching point of the streamline that follows the wind. The magnetocentrifugal winds can produce both very highly collimated jets and slow wide-angle disk winds. Their kinematics and morphology depend on the thermal effects on the launching regions. Numerical simulations (e.g., Bai et al. 2016) show that for low values of λ, magnetocentrifugal winds can extract significant mass and angular momentum from the disk.

As mentioned above, we assume that the three shells of HH 30 are driven by disk winds associated with three different episodic ejections. Under this assumption, the asymptotic values of the poloidal velocity V_p and the specific angular momentum for each streamline are (Blandford & Payne 1982)

$$V_p = \sqrt{2\lambda - 3}\,\sqrt{GM_*/r_0}, \tag{9}$$

$$R \times v_\phi = \lambda\sqrt{GM_* r_0}. \tag{10}$$

Figure 13 shows the relation between the specific angular momentum $j = R \times v_\phi$ and the poloidal velocity V_p for the

[8] The pseudo-pulse effects are perturbations in density, poloidal velocity, pressure, and magnetic field strength produced by oscillations in magnetic forces (Shang et al. 2020).

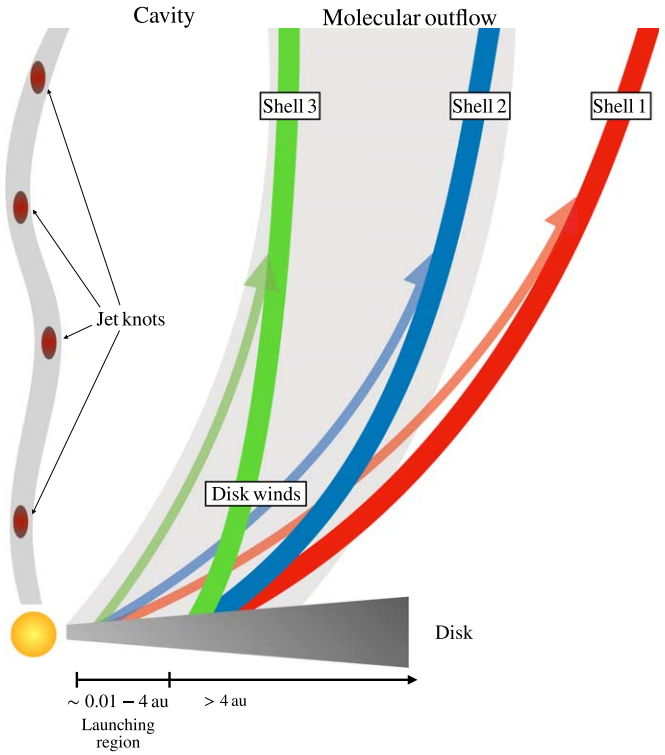

Figure 12. Schematic scenario of the different components of source HH 30 under the assumption that the outflow is driven by disk winds.

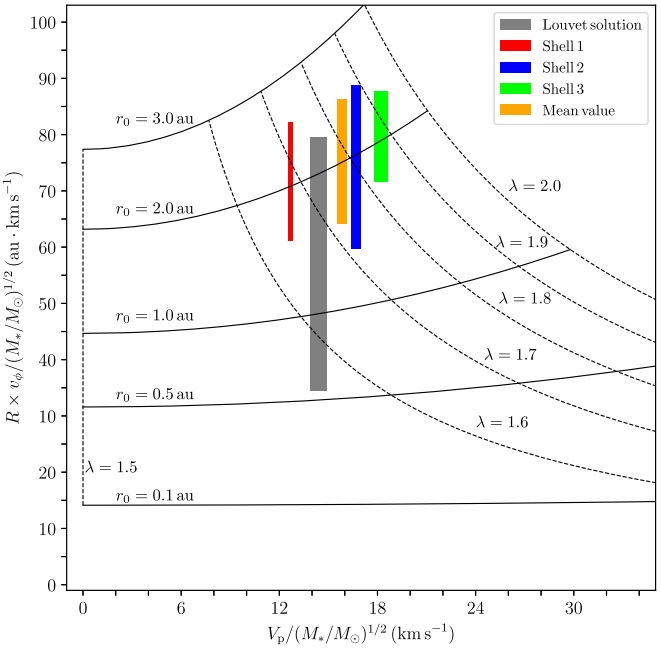

Figure 13. Specific angular momentum as a function of the poloidal velocity for steady and axisymmetric MHD disk winds, both normalized to $\sqrt{M_*}$. The black lines represent the expected relation from self-similar cold magnetocentrifugal disk winds with r_0 from 0.01 to 3 au and λ from 1.5 to 1.8 (Ferreira et al. 2006). The red, blue, and green rectangles show the mean value for shells 1, 2, and 3, respectively. The orange rectangle is the mean value of λ of the three shells. The gray rectangle corresponds to the solution for the outflow HH 30 of Louvet et al. (2018).

various solutions of the launching point r_0 and magnetic lever arm parameter λ. The mean poloidal velocities and the mean specific angular momentum from the three shells follow the line of $r_0 = 2$ au and $\lambda \sim 1.6$–1.9. For the three shells, the launching radii r_0 are consistent with our estimates through Anderson's relation for $R_{\rm launch}$, and our assumption that the three shells are launched from the same region is confirmed. Also, the low derived limit on $\lambda \sim 1.6$–1.9 is consistent with a solution for warm magnetohydrodynamic disk wind models (Casse & Ferreira 2000) or cold magnetohydrodynamic disk wind models from weakly magnetized disks (Jacquemin-Ide et al. 2019). The gray rectangle of Figure 13 represents the solution derived by Louvet et al. (2018) for HH 30.

In Section 3.4, we estimated a mass of $(1.83 \pm 0.19) \times 10^{-4}\,M_\odot$ for the HH 30 outflow. For simplicity, we assume that the outward $V_z = 12.2 \pm 0.5$ km s^{-1}, poloidal $V_p = 12.8 \pm 0.5$ km s^{-1}, and rotation $v_\phi = 0.13 \pm 0.04$ km s^{-1} velocities correspond to the values for shell 3 at a height of $z = 4\farcs8 \approx 672$ au, under the assumption that these velocities tend to be constant at large heights. The size of the molecular outflow is 19″ with a cylindrical radius of $R = 394 \pm 20$ au (estimated with the general relation $z = aR^{-\beta/2}$ shown in Section 3.3). We obtain a dynamical time $\tau_{\rm dyn} = z/V_z = (1.04 \pm 0.07) \times 10^3$ yr, a mass-loss rate of the outflow of $\dot{M}_{\rm outflow} = M_{\rm outflow}/\tau_{\rm dyn} \approx (1.76 \pm 0.21) \times 10^{-7}\,M_\odot$ yr^{-1}, a linear momentum rate of $\dot{P}_{\rm outflow} = \dot{M}_{\rm outflow} V_{\rm p} \approx (2.25 \pm 0.29) \times 10^{-6}\,M_\odot$ yr^{-1} km s^{-1}, and an angular momentum rate of $\dot{L}_{\rm outflow} = \dot{M}_{\rm outflow} R v_\phi = (9 \pm 2.9) \times 10^{-6}\,M_\odot$ yr^{-1} au km s^{-1}.

The mass-loss rate of the HH 30 wind, $\dot{M}_w \simeq 9 \times 10^{-8}\,M_\odot$ yr^{-1} (Louvet et al. 2018), is smaller than the mass-loss rate of the outflow by a factor $\dot{M}_{\rm outflow}/\dot{M}_w \sim 1.95 \pm 0.24$.

If we assume that the outflow is a disk wind with $\dot{M}_{\rm outflow} = \dot{M}_w \sim f\dot{M}_{\rm d,a}$, we can estimate the accretion luminosity at the stellar surface as

$$L_a = \eta \frac{GM_* \dot{M}_{\rm d,a}}{R_*} \equiv \eta \frac{GM_* \dot{M}_{\rm outflow}}{fR_*}, \qquad (11)$$

where R_* is the stellar radius and $\eta \sim 0.5$. Using $M_* = (0.45 \pm 0.14)\,M_\odot$ and $R_* \sim 2$–$3\,R_\odot$, the accretion luminosity is $L_a \geqslant (1/f)(0.41 \pm 0.14 - 0.62 \pm 0.21)\ L_\odot$. This value is consistent with the luminosity of the source of 0.2–0.9 $L_\odot$ (Cotera et al. 2001) by a factor of $f \sim 0.6$–2.

Under a scenario of all mass and angular momentum being removed from the accretion disk by magnetocentrifugal disk winds, the lever arm relates the mass-loss rate with the disk accretion rate as $\dot{M}_w \sim \dot{M}_{\rm acc}/\lambda$ (Pelletier & Pudritz 1992). This assumption is consistent with the λ values found for the three shells and with the f value found for the accretion luminosity.

In summary, the λ values found, the estimated rates of the outflow and the disk wind, and the accretion luminosity argue in favor of the scenario with multiple shells driven by a disk wind.

5. Conclusions

We present a detailed analysis of ALMA archival observations for the molecular line emission from ^{13}CO and ^{12}CO from the accretion disk and the molecular outflow, respectively, associated with the protostellar system HH 30. Our main results are the following.

1. The emission from ^{13}CO traces the accretion disk, which presents Keplerian rotation. We estimate the dynamical mass of the central object of the system (central protostar and disk mass) as $M_{\rm dyn} = 0.45 \pm 0.14\,M_\odot$.

2. We identify the internal cavity in the molecular outflow, where the emission from ^{12}CO traces the walls of this cavity. Furthermore, the high velocity of the gas between the $S_{[II]}$ knots of the precessing jet could imply that the molecular outflow is a combination of the material entrained by the jet and the disk winds launched directly from the accretion disk.
3. The position–velocity diagrams perpendicular to the jet axis show a structure with multiple internal shells. We detect three different shells associated with the episodic ejections of a wide-angle wind from the accretion disk. The dynamical ages of the shells are $\sim 497 \pm 15$ yr (shell 1), $\sim 310 \pm 9$ yr (shell 2), and $\sim 262 \pm 11$ yr (shell 3). The difference between the first and second events is $\sim 187 \pm 17$ yr, and that between the second and last events is $\sim 48 \pm 14$ yr.
4. The kinematics of the different shells show that the three shells are in constant expansion in the radial direction and present signatures of rotation.
5. Our estimations of the launching radii, 2 ± 2 au, and the magnetic lever arm, $\lambda \sim 1.6$–1.9, of the three shells are consistent with the values expected if the molecular outflow is launched through magnetocentrifugal processes.
6. The lower limit of the mass of the molecular outflow is $M_{\rm outflow} = (1.83 \pm 0.19) \times 10^{-4}\, M_{\odot}$, with a mass-loss rate of $(1.76 \pm 0.21) \times 10^{-7}\, M_{\odot}\, {\rm yr}^{-1}$, linear momentum rate of $(2.25 \pm 0.29) \times 10^{-6}\, M_{\odot}\, {\rm yr}^{-1}\, {\rm km\, s}^{-1}$, and an angular rate of $(9 \pm 2.9) \times 10^{-6}\, M_{\odot}\, {\rm yr}^{-1}\, {\rm km\, s}^{-1}$ au. As a result of the comparison of these rates with the mass and the linear and angular momentum of the wind, we find that these rates are very similar. We also found that the accretion luminosity is consistent with the luminosity of the central source by a factor of $f \sim 0.6$–2.
7. The dynamical times, the launching radii, and the magnetic lever arm of the three shells, as well as the mass and the linear and angular momentum rates of the outflow, are strong evidence that the molecular outflow associated with the HH 30 system originates from episodic ejections of a slow wide-angle disk wind.

Acknowledgments

We thank an anonymous referee for very useful suggestions that improved the presentation of this paper. J. A. López-Vázquez and Chin-Fei Lee acknowledge grants from the National Science and Technology Council of Taiwan (NSTC 110–2112–M–001–021–MY3 and 112–2112–M–001–039–MY3) and the Academia Sinica (Investigator Award AS–IA–108–M01). L.A.Z. acknowledges financial support from CONACyT-280775 and UNAM-PAPIIT IN110618, and IN112323 grants, México. This paper makes use of the following ALMA data: ADS/JAO.ALMA#2013.1.01175.S and ADS/JAO.ALMA#2018.1.01532.S. ALMA is a partnership of ESO (representing its member states), NSF (USA) and NINS (Japan), together with NRC (Canada), MOST and ASIAA (Taiwan), and KASI (Republic of Korea), in cooperation with the Republic of Chile. The Joint ALMA Observatory is operated by ESO, AUI/NRAO and NAOJ.

Appendix

In this Appendix we include the complete velocity cube with 0.3 km s^{-1} width channel of the molecular outflow associated with HH 30. Figure 14 shows the blueshifted channel maps while the redshifted channel maps are presented in Figure 15. The position velocity diagrams perpendicular to the jet axis to high heights ($z \geq 6''$) are shown in Figure 16. The fact that shells 1 and 2 are not detected may be associated with expansion and coolling effects of the CO.

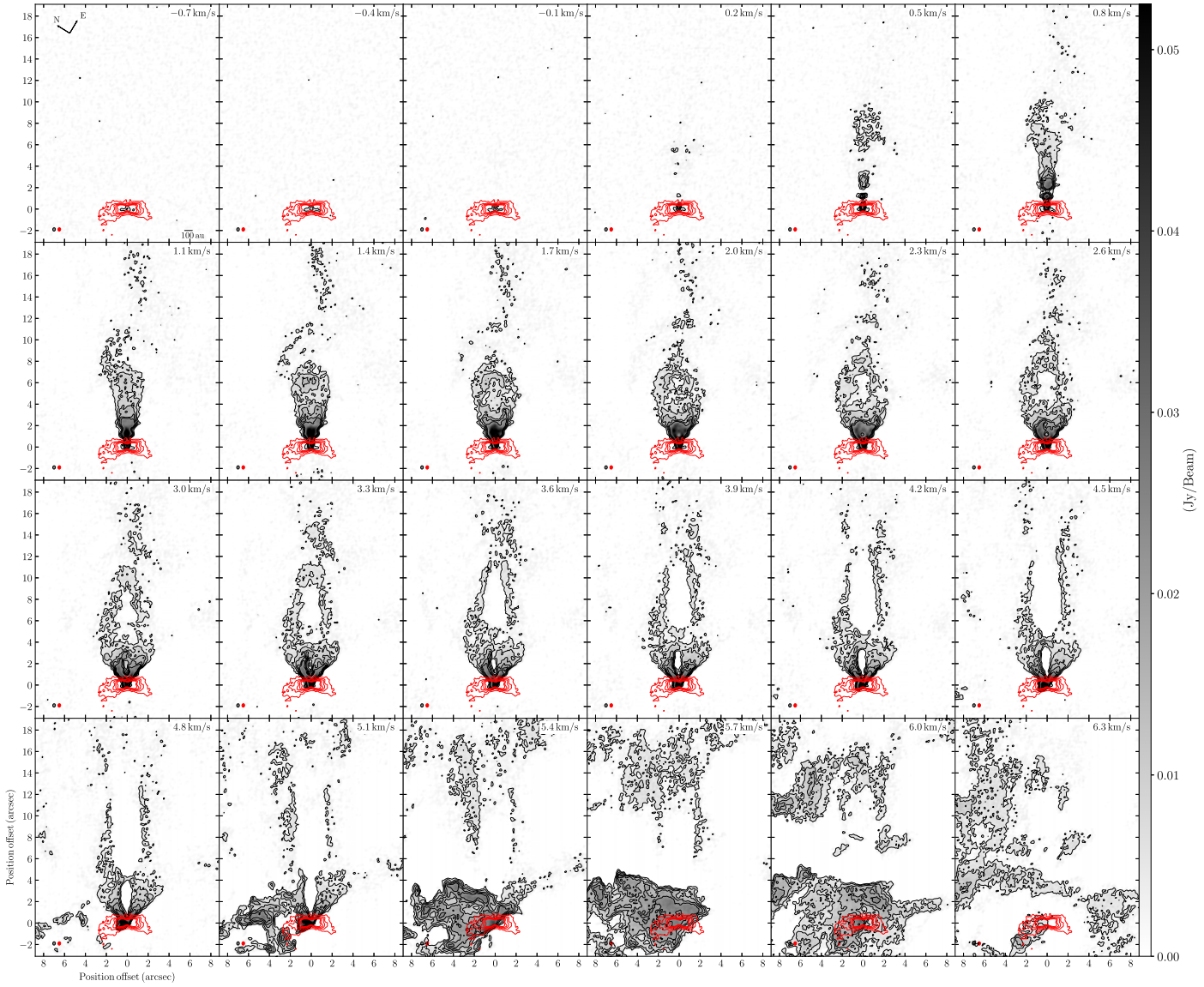

Figure 14. Blueshifted channel maps of the ^{12}CO molecular line emission of the molecular outflow of HH 30. The channel velocity is indicated at the top right. The contours levels start from 3σ with steps of 5σ, 10σ, 15σ, and 20σ, where $\sigma = 0.96$ Jy beam^{-1}. The red contours correspond to the moment zero (integrated intensity) of the HH 30 disk emission from the ^{13}CO molecular line; the contours levels start from 5σ in steps of 5σ, 10σ, 15σ, and 20σ, where $\sigma = 1.07 \times 10^{-3}$ Jy beam^{-1}. The synthesized beams in all panels are shown in the lower left corner.

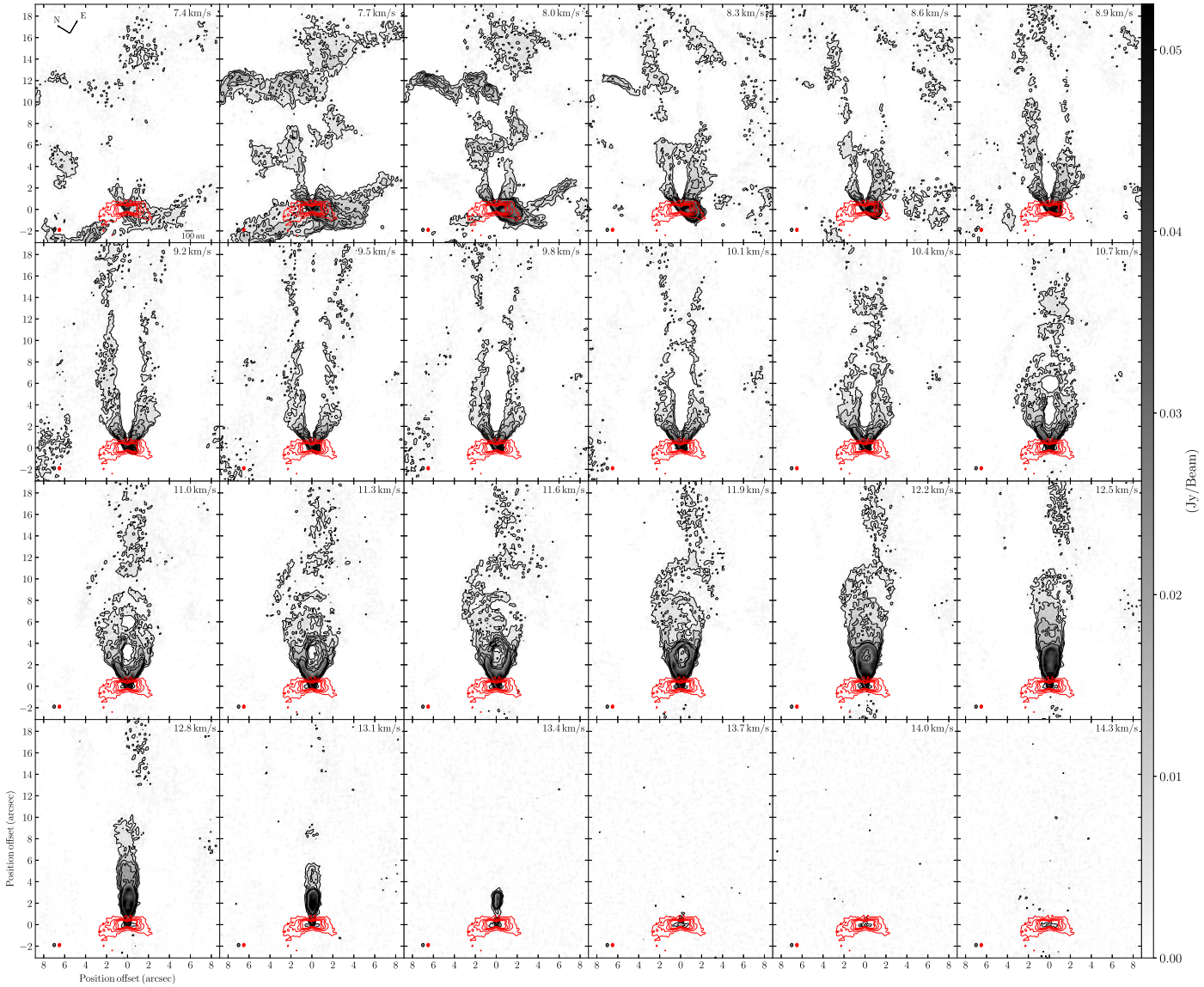

Figure 15. Redshifted channel maps of the ^{12}CO molecular line emission of the molecular outflow of HH 30. The description is the same as for Figure 14.

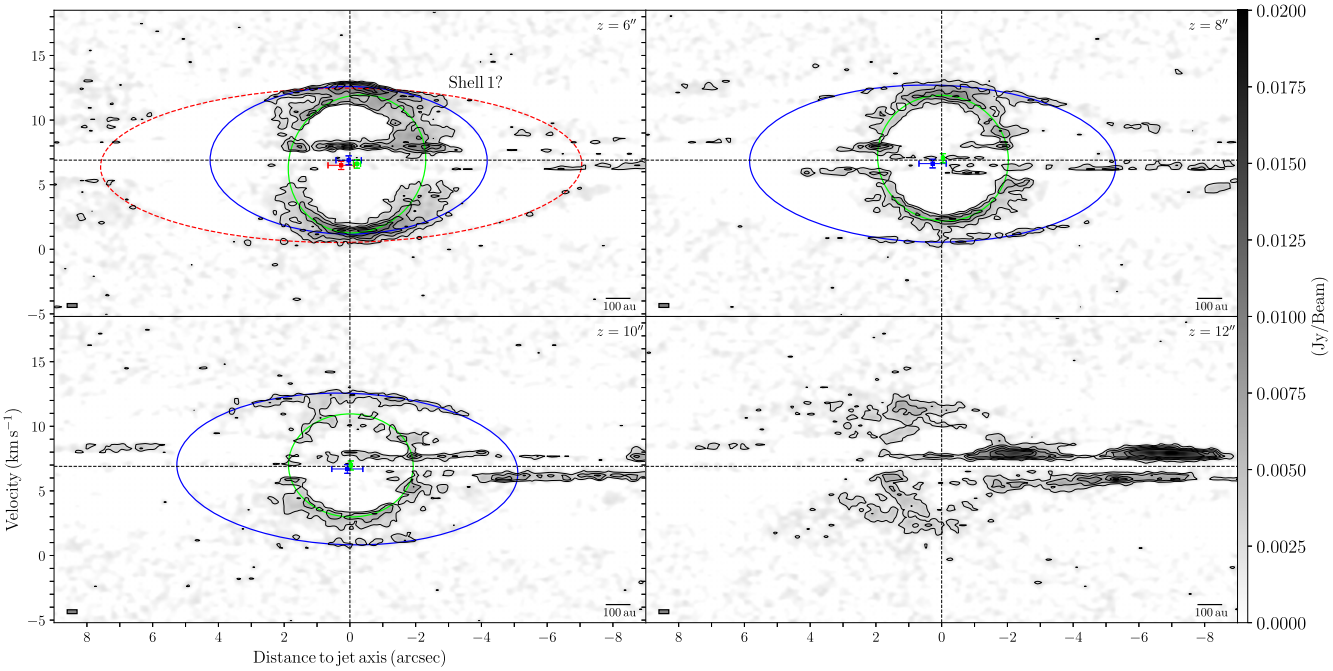

Figure 16. Position–velocity diagrams from ^{12}CO emission perpendicular to the jet axis at different heights from $z = 6''$ (840 au) to $z = 12''$ (1680 au) with intervals of $2''$ (280 au). The description is the same as for Figure 5.

ORCID iDs

J. A. López-Vázquez https://orcid.org/0000-0002-5845-8722
Chin-Fei Lee https://orcid.org/0000-0002-3024-5864
M. Fernández-López https://orcid.org/0000-0001-5811-0454
Fabien Louvet https://orcid.org/0000-0003-3814-4424
O. Guerra-Alvarado https://orcid.org/0000-0003-4753-8759
Luis A. Zapata https://orcid.org/0000-0003-2343-7937

References

Alexander, R., Pascucci, I., Andrews, S., Armitage, P., & Cieza, L. 2014, in Protostars and Planets VI, ed. H. Beuther et al. (Tucson, AZ: Univ. Arizona Press), 475
Anderson, J. M., Li, Z.-Y., Krasnopolsky, R., & Blandford, R. D. 2003, ApJL, 590, L107
Anglada, G., López, R., Estalella, R., et al. 2007, AJ, 133, 2799
Arce, H. G., Borkin, M. A., Goodman, A. A., Pineda, J. E., & Beaumont, C. N. 2011, ApJ, 742, 105
Arce, H. G., & Sargent, A. I. 2006, ApJ, 646, 1070
Aso, Y., Ohashi, N., Saigo, K., et al. 2015, ApJ, 812, 27
Aso, Y., & Sai, J. 2023, jinshisai/SLAM: First Release of SLAM, v1.0.0, Zenodo, doi:10.5281/zenodo.7783868
Bai, X.-N., & Stone, J. M. 2017, ApJ, 836, 46
Bai, X.-N., Ye, J., Goodman, J., & Yuan, F. 2016, ApJ, 818, 152
Bjerkeli, P., van der Wiel, M. H. D., Harsono, D., Ramsey, J. P., & Jørgensen, J. K. 2016, Natur, 540, 406
Blandford, R. D., & Payne, D. G. 1982, MNRAS, 199, 883
Booth, A. S., Tabone, B., Ilee, J. D., et al. 2021, ApJS, 257, 16
Caratti o Garatti, A., Garcia Lopez, R., Antoniucci, S., et al. 2012, A&A, 538, A64
CASA Team, Bean, B., & Bhatnagar, S. 2022, PASP, 134, 114501
Casse, F., & Ferreira, J. 2000, A&A, 353, 1115
Cotera, A. S., Whitney, B. A., Young, E., et al. 2001, ApJ, 556, 958
de Valon, A., Dougados, C., Cabrit, S., et al. 2020, A&A, 634, L12
de Valon, A., Dougados, C., Cabrit, S., et al. 2022, A&A, 668, A78
Ellerbroek, L. E., Podio, L., Kaper, L., et al. 2013, A&A, 551, A5
Estalella, R., López, R., Anglada, G., et al. 2012, AJ, 144, 61
Evans, N. J., I, Dunham, M. M, Jørgensen, J. K., et al. 2009, ApJS, 181, 321
Federman, S., Megeath, S. T., Rubinstein, A. E., et al. 2023, arXiv:2310.03803
Fernández-López, M., Girart, J. M., Curiel, S., et al. 2013, ApJ, 778, 72
Fernández-López, M., Zapata, L. A., Rodríguez, L. F., et al. 2020, AJ, 159, 171
Ferreira, J., Dougados, C., & Cabrit, S. 2006, A&A, 453, 785
Frank, A., Ray, T. P., Cabrit, S., et al. 2014, in Protostars and Planets VI, ed. H. Beuther et al. (Tucson, AZ: Univ. Arizona Press), 451
Hirota, T., Machida, M. N., Matsushita, Y., et al. 2017, NatAs, 1, 0146
Hsieh, T.-H., Lai, S.-P., & Belloche, A. 2017, AJ, 153, 173
Jacquemin-Ide, J., Ferreira, J., & Lesur, G. 2019, MNRAS, 490, 3112
Konigl, A., & Pudritz, R. E. 2000, in Protostars and Planets IV, ed. V. Mannings, A. P. Boss, & S. S. Russell (Tucson, AZ: Univ. Arizona Press), 759
Launhardt, R., Pavlyuchenkov, Y., Gueth, F., et al. 2009, A&A, 494, 147
Launhardt, R., Pavlyuchenkov, Y. N., Akimkin, V. V., et al. 2023, A&A, 678, A135
Lee, C.-F. 2020, A&ARv, 28, 1
Lee, C.-F., Ho, P. T. P., Li, Z.-Y., et al. 2017, NatAs, 1, 0152
Lee, C.-F., Ho, P. T. P., Palau, A., et al. 2007, ApJ, 670, 1188
Lee, C.-F., Mundy, L. G., Reipurth, B., Ostriker, E. C., & Stone, J. M. 2000, ApJ, 542, 925
Lee, C.-F., Stone, J. M., Ostriker, E. C., & Mundy, L. G. 2001, ApJ, 557, 429
Lee, C.-F., Li, Z.-Y., Codella, C., et al. 2018, ApJ, 856, 14
López-Vázquez, J. A., Cantó, J., & Lizano, S. 2019, ApJ, 879, 42
López-Vázquez, J. A., Zapata, L. A., & Lee, C.-F. 2023, ApJ, 944, 63
López-Vázquez, J. A., Zapata, L. A., Lizano, S., & Cantó, J. 2020, ApJ, 904, 158
Louvet, F., Dougados, C., Cabrit, S., et al. 2018, A&A, 618, A120
Mitchell, G. F., Hasegawa, T. I., Dent, W. R. F., & Matthews, H. E. 1994, ApJL, 436, L177
Pascucci, I., Cabrit, S., Edwards, S., et al. 2022, arXiv:2203.10068
Pech, G., Zapata, L. A., Loinard, L., & Rodríguez, L. F. 2012, ApJ, 751, 78
Pelletier, G., & Pudritz, R. E. 1992, ApJ, 394, 117
Pety, J., Gueth, F., Guilloteau, S., & Dutrey, A. 2006, A&A, 458, 841
Plunkett, A. L., Arce, H. G., Mardones, D., et al. 2015, Natur, 527, 70
Podio, L., Eislöffel, J., Melnikov, S., Hodapp, K. W., & Bacciotti, F. 2011, A&A, 527, A13
Podio, L., Tabone, B., Codella, C., et al. 2021, A&A, 648, A45
Pudritz, R. E., & Norman, C. A. 1986, ApJ, 301, 571
Pudritz, R. E., Ouyed, R., Fendt, C., & Brandenburg, A. 2007, in Protostars and Planets V, ed. B. Reipurth, D. Jewitt, & K. Keil (Tucson, AZ: Univ. Arizona Press), 277
Ray, T. P., McCaughrean, M. J., Caratti o Garatti, A., et al. 2023, Natur, 622, 48

Sai, J., Ohashi, N., Saigo, K., et al. 2020, ApJ, 893, 51
Seale, J. P., & Looney, L. W. 2008, ApJ, 675, 427
Seifried, D., Sánchez-Monge, Á., Walch, S., & Banerjee, R. 2016, MNRAS, 459, 1892
Shang, H., Krasnopolsky, R., Liu, C.-F., & Wang, L.-Y. 2020, ApJ, 905, 116
Shang, H., Liu, C.-F., Krasnopolsky, R., & Wang, L.-Y. 2023, ApJ, 944, 230
Shu, F., Najita, J., Galli, D., Ostriker, E., & Lizano, S. 1993, in Protostars and Planets III, ed. E. H. Levy & J. I. Lunine (Tucson, AZ: Univ. Arizona Press), 3
Shu, F. H., Najita, J. R., Shang, H., & Li, Z. Y. 2000, in Protostars and Planets IV, ed. V. Mannings, A. P. Boss, & S. S. Russell (Tucson, AZ: Univ. Arizona Press), 789
Stanke, T., Arce, H. G., Bally, J., et al. 2022, A&A, 658, A178
Suriano, S. S., Li, Z.-Y., Krasnopolsky, R., & Shang, H. 2017, MNRAS, 468, 3850
Suriano, S. S., Li, Z.-Y., Krasnopolsky, R., & Shang, H. 2018, MNRAS, 477, 1239
Suriano, S. S., Li, Z.-Y., Krasnopolsky, R., Suzuki, T. K., & Shang, H. 2019, MNRAS, 484, 107
Tabone, B., Cabrit, S., Pineau des Forêts, G., et al. 2020, A&A, 640, A82
Ulrich, R. K. 1976, ApJ, 210, 377
Velusamy, T., Langer, W. D., & Thompson, T. 2014, ApJ, 783, 6
Villenave, M., Ménard, F., Dent, W. R. F., et al. 2020, A&A, 642, A164
Wang, L., Bai, X.-N., & Goodman, J. 2019, ApJ, 874, 90
Wright, M., Bally, J., Hirota, T., et al. 2022, ApJ, 924, 107
Zapata, L. A., Arce, H. G., Brassfield, E., et al. 2014, MNRAS, 441, 3696
Zapata, L. A., Lizano, S., Rodríguez, L. F., et al. 2015, ApJ, 798, 131
Zapata, L. A., Loinard, L., Schmid-Burgk, J., et al. 2011, ApJL, 726, L12
Zapata, L. A., Schmid-Burgk, J., Muders, D., et al. 2010, A&A, 510, A2
Zhang, Y., Arce, H. G., Mardones, D., et al. 2016, ApJ, 832, 158
Zhang, Y., Arce, H. G., Mardones, D., et al. 2019, ApJ, 883, 1
Zhang, Y., Higuchi, A. E., Sakai, N., et al. 2018, ApJ, 864, 76
Zucker, C., Speagle, J. S., Schlafly, E. F., et al. 2019, ApJ, 879, 125